



Harnessing electroacoustic analogies in designing acoustic topological systems

Hasan Al Ba'ba'a^{1,2}, Kyung Hoon Lee², and Qiming Wang²

 ¹Department of Mechanical Engineering, Union College, Schenectady, NY 12308, USA

²Sonny Astani Department of Civil and Environmental Engineering, University of Southern California, Los Angeles, CA 90089, USA

 albabaah@union.edu

Topological acoustics has recently witnessed a spurt in research activity, owing to their unprecedented properties that extend beyond the standard wave dispersion for vibration control. In recent years, the use of coupled arrays of acoustic chambers has gained popularity in designing acoustic topological systems. In their common form, acoustic chambers with relatively large volume are coupled with others via narrow channels. Such configuration generally necessitates modeling in full three-dimensional model and may require extended computational time for simulation their harmonic response. To this end, this paper establishes a comprehensive mathematical treatment of the use of electroacoustic analogies for designing acoustic topological systems. We demonstrate the potential of such analytical approach via two types of topological systems: (1) edge states with quantized winding numbers in an acoustic diatomic lattice and (2) valley Hall transition in an acoustic honeycomb lattice that leads to robust waveguiding. In both cases, the established analytical approach shows an excellent agreement with the full three-dimensional model, whether in dispersion analyses or the response of an acoustic system with finite number of cells. The established framework opens avenues for designing a verity of acoustic topological insulators with simplified analytical formulation and minimal computational costs.

Keywords

Topological Insulators; Acoustic Lattices; Electroacoustic Analogies; Quantum Valley Hall Effect; Edge states.

1 Introduction

The study of topological acoustics has recently witnessed a spurt in research activity, owing to their unprecedented properties that extend beyond the standard wave dispersion for vibration control. A variety of emerging phenomena including robustness against defects, unidirectionality in wave transmission, and backscattering-immunity have been recently demonstrated [1, 2]. Such interesting behaviours have given rise to various applications with inherent topological protection, such as robust wave guiding and one-way signal transport[3, 4], logic operations[5], and negative refraction[6].

In recent years, the use of coupled arrays of acoustic chambers has gained popularity in designing acoustic topological insulators [7–13]. In their common form, acoustic chambers with relatively large volume are coupled with their neighboring chambers via narrow channels in a single or multiple directions, which will be referred to as *acoustic lattices* henceforth. The fascinating part of using these acoustic lattices is their ability to closely mimic Hamiltonians pertaining to a variety of topological system types in analogy to electronic systems. To date, coupled acoustic chambers have been used in inducing robust edge states [7, 8], Quantum Valley Hall Effect (QVHE) [9, 10], Quantum Spin Hall Effect (QSHE) [10], Hofstadter-butterfly effect in quasi-periodic lattices [11] and, more recently, higher order topological insulators with corner states [12–14]. Owing to the three-dimensional nature of such acoustic lattices, numerical modeling is often achieved via finite-element based procedure, and the effective Hamiltonians are commonly established via parameter fitting of the coupling [7]. In addition, electroacoustic analogies (circuit lumped-parameter model) have also been demonstrated as a suitable methodology for modeling Hamiltonians of an acoustic Kagome lattice [15], among other examples in literature [16–20].

In light of the aforementioned studies, we aim to establish a comprehensive analytical framework for acoustic lattices using electroacoustic analogies to ultimately design non-trivial topological states. The key importance of such approach is two-fold: (i) to provide an analytical insight into the topological protection mechanism in acoustic lattices and (ii) to reduce computational cost for analyzing them. While modeling acoustic lattices via harnessing lumped circuit equivalents is convenient in terms of fast calculation and obtaining analytical models, the approach becomes less accurate as the frequency gets higher[15, 17]. Nonetheless, as will be shown, the first few dispersion branches and their corre-

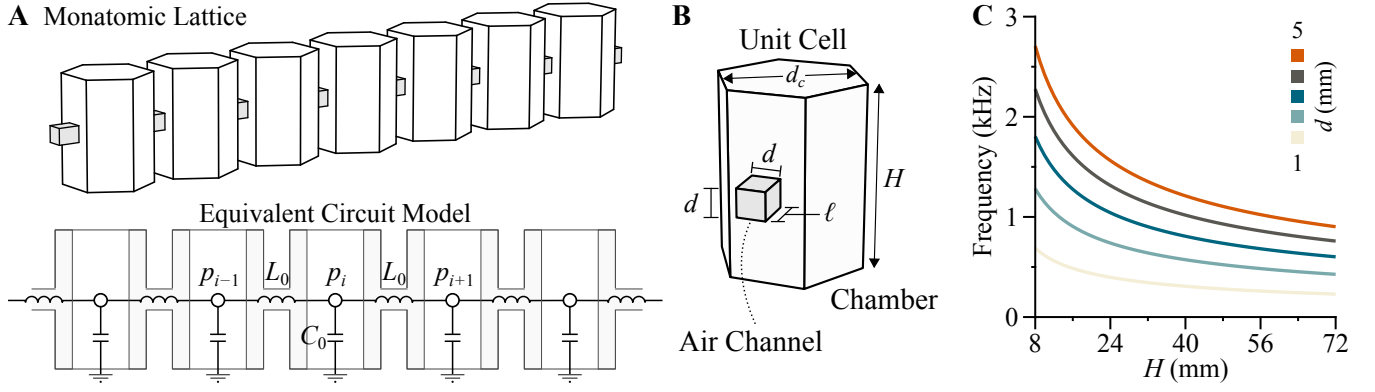


Figure 1: (A) Schematic for a monatomic acoustic lattice and its equivalent electrical model. (B) Unit cell of the monatomic lattice detailing the geometrical properties of the chamber and channel. (C) Fundamental frequency of an isolated unit cell (acting as a Helmholtz resonator) with varying chamber height H and square channel side d . The length of the air channel and hexagon's side remain unchanged and are chosen to be $\ell = 4\text{mm}$ and $d_c = 14\text{mm}$, respectively.

sponding frequency response in a finite acoustic lattice can be estimated with relatively high accuracy, rendering such a methodology an asset in studying topological acoustic systems with high computational efficiency.

To illustrate the concept, we start by studying an acoustic monatomic lattice to establish variables and physical meanings of coupled chambers. Established circuit analogues typically consist of a series of coupled inductors and grounded capacitors, whose inductance and capacitance are estimated based on the geometrical properties. The parameters of the dispersion relations are interpreted based on the renowned Helmholtz resonance, which enable a better estimation of resonance frequencies based on the geometry of acoustic system. Afterwards, and based on the established understanding of acoustic monatomic lattices, we present two types of topological acoustic systems: (1) a diatomic lattice with non-vanishing quantized winding number and edge states, and (2) a honeycomb lattice with QVHE for designing robust waveguides. The developed circuit model for both lattices is compared with the numerical results from a full-scale three-dimensional counterpart in regards of dispersion analysis and a lattice with a finite number of cells. In addition, we show how to correctly account for the boundary conditions and implement the right correction parameters for the equivalent length of air channels at lattice boundaries, resulting in a more accurate predication of system's resonances.

2 Acoustic monatomic lattices

2.1 Electroacoustic analogies: Modeling and geometrical dependence

We start by demonstrating the electroacoustic analogy in a chain of identical acoustic chambers (or cavities) coupled via narrow channels with rigid walls to satisfy sound hard boundaries (Fig. 1A,B). We shall refer to this chain as an *acoustic monatomic lattice* due to its resemblance to a typical monatomic lattice as will be shown shortly. At relatively low frequencies, the acoustic pressure inside each of these chambers is assumed to be constant throughout, thus constituting its only degree of freedom, denoted here as p_i with i symbolizing the chamber's order in the acoustic chain (Fig. 1A). As a result, electroacoustic analogies can be readily utilized and offer intriguing mapping of acoustic pressure and particle velocity in acoustic medium to voltage and current in circuitry [17]. In fact, narrow channels and acoustic chambers are analogous to electric inductors with inductance L_0 and grounded capacitors of capacitance C_0 , respectively, and their values are estimated based on chamber/channel geometrical properties [17]:

$$L_0 = \frac{\rho \ell_e}{S} \quad (1a)$$

$$C_0 = \frac{V}{\rho c^2} \quad (1b)$$

Here, S is the cross-sectional area of the narrow channel, ρ is the fluid's density, V is the chamber's volume, c is the sound speed in the fluid medium, and ℓ_e is the effective length of channels (which is often longer than the channel's physical length ℓ).

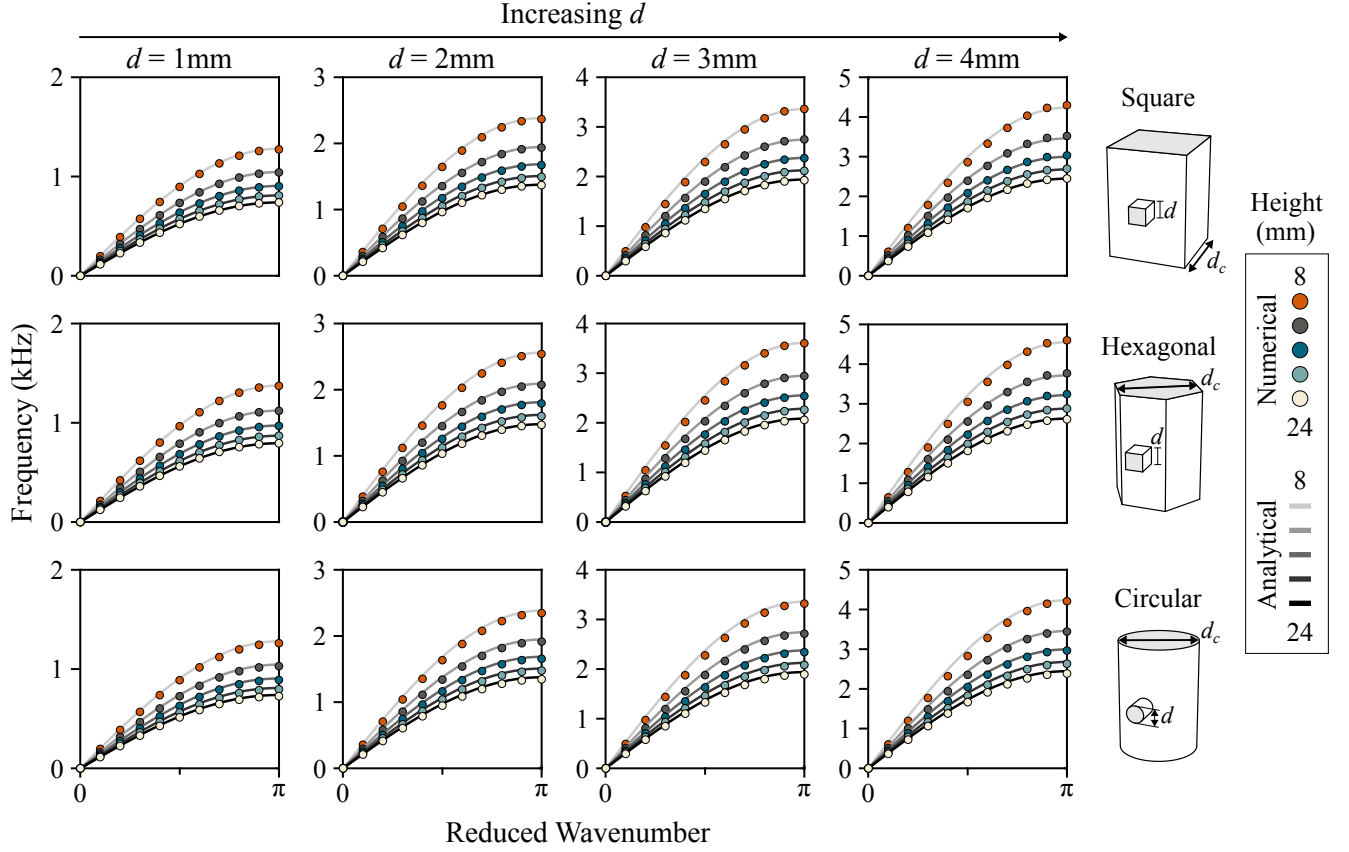


Figure 2: Dispersion relation of acoustic monatomic lattices with different combination of parameters and geometrical shapes. The plots show the analytically obtained dispersion relation from the electrical acoustic model (color-coded lines) in comparison to the full-scale three-dimensional model simulated via commercial software COMSOL (color-coded circles).

2.2 Dispersion relation and relevance to Helmholtz resonance

The equivalence of the acoustic monatomic lattice to a circuit model is intended to derive a simplified analytical expression of dispersion relation to avoid analyzing lattice's full-scale three-dimensional unit cell. From electrical circuit analysis, the electrical current is induced via a change in voltage across an electrical element. Assuming harmonic motion, the current I flowing through inductors (capacitors), in response to a drop in voltage ΔV , is governed by the reciprocal of a frequency-dependent impedance $Z_0 = i\omega L_0$ ($Z_0 = 1/(i\omega C_0)$), yielding $I = \Delta V / Z_0$ (i is the imaginary unit). Exploiting the mapping of pressure to voltage and knowing that currents entering and exiting a junction sum to zero (per Kirchhoff law), the governing equation of the i th acoustic chamber is:

$$\left(\frac{2}{i\omega L_0} + i\omega C_0 \right) p_i - \frac{1}{i\omega L_0} (p_{i+1} + p_{i-1}) = 0 \quad (2)$$

Applying Bloch theorem $p_{i\pm 1} = p_i e^{\pm i\mu}$ and multiplying by $i\omega L_0$, further symbolic computations yield the dispersion relation:

$$\omega = 2\omega_0 \left| \sin \left(\frac{\mu}{2} \right) \right| \quad (3)$$

where μ is the non-dimensional wavenumber and:

$$\omega_0 = \sqrt{\frac{1}{L_0 C_0}} \quad (4)$$

Equation (3) is in perfect analogy with the dispersion relation of a typical elastic monatomic lattice, albeit with the definition of ω_0 being the natural frequency of a spring-mass system[21]. For our acoustic lattice, we interpret the quantity ω_0 in Equation (4) as the natural frequency of a stand-alone Helmholtz resonator (an isolated unit cell as seen in Fig. 1B), owing to the fact that a Helmholtz resonator is often mapped to a spring-mass system[22–24]. Consequently,

an acoustic monatomic lattice can be perceived as serially coupled Helmholtz resonators. Implementing this physical understanding, in addition, facilitates a better estimation of acoustic lattice properties. For example, the effective length ℓ_e for a Helmholtz resonator is suggested to be:

$$\ell_e = \ell(1 + \delta_c) \quad (5)$$

The correction factor δ_c is the summation of the inner and outer end corrections, which are chosen here as $\delta_{\text{in}} = 0.425d_h/\ell$ and $\delta_{\text{out}} = 0.3d_h/\ell$, respectively, for flanged and unflanged ends[25]. Accordingly, the complete correction factor is $\delta_c = 0.725d_h/\ell$, with $d_h = 4S/P$ (P is the channel's perimeter) is defined herein as the channel's hydraulic diameter[26]. Note that the hydraulic diameter for a square (circular) channel is equal to the channel's side length (nominal diameter). Making use of Equations (1), (4), and (5), the Helmholtz resonance can be explicitly expressed in terms of the resonator's geometrical properties in units of Hertz:

$$f_R = \frac{\omega_0}{2\pi} = \frac{c}{2\pi\ell} \sqrt{\frac{V_c/V}{1 + \delta_c}} \quad (6)$$

where V_c is the volume of the channel. Equation (6) implies that the larger the ratio of the volumes, the larger the natural frequency, given a constant length ℓ (Fig. 1C). Doubling this quantity provides an estimate for the cutoff frequency (in Hz) of the acoustic monatomic lattice, as inferred from Equation (3).

2.3 Numerical examples

We simulate three different combinations of the acoustic chamber/channel's geometrical cross-sectional areas: (1) square chambers with square channels, (2) hexagonal chambers with square channels, and, (3) circular chambers with circular channels (Fig. 2). Three-dimensional model simulations are done via COMSOL commercial software and assuming a discretization of the Quadratic Lagrange type. For distinction between the circuit model and the full three-dimensional model, we shall label the dispersion relation or related system dynamics obtained from the circuit model as *analytical*, while the one obtained from COMSOL simulations as *numerical*. Calculating the dispersion relation for a swept range of the hydraulic diameter d and height H , while maintaining the length $\ell = 4\text{mm}$ and parameter $d_c = 14\text{mm}$ (from which the area S is calculated) constant throughout, we observe that all analytical dispersion relations closely resemble their numerical counterparts (Fig. 2). As such, it is now evident that Equation (6) can effectively estimate the natural frequency of the stand-alone Helmholtz resonator with excellent accuracy, and consequently producing the most fitting dispersion relation per Equation (3). This also displays the competence of the circuit model in predicting the dispersion relation while maintaining very low computational cost relative to the three-dimensional model.

3 Acoustic diatomic lattices

3.1 Mathematical formulation and dispersion analysis

Next, we consider an acoustic diatomic lattice constituting an array of equally sized acoustic chambers, coupled via alternating narrow/wide channels with hydraulic diameters d_1 and d_2 (Fig. 3). We shall demonstrate the emergence of edge states via analyzing the band topology associated with the unit cell of the diatomic lattice. Analogous to the analysis of the acoustic monatomic lattice, the governing equations of a diatomic unit cell are derived:

$$\left(\frac{1}{i\omega L_1} + \frac{1}{i\omega L_2} + i\omega C \right) p_i - \left(\frac{1}{i\omega L_1} q_i + \frac{1}{i\omega L_2} q_{i-1} \right) = 0 \quad (7a)$$

$$\left(\frac{1}{i\omega L_1} + \frac{1}{i\omega L_2} + i\omega C \right) q_i - \left(\frac{1}{i\omega L_1} p_i + \frac{1}{i\omega L_2} p_{i+1} \right) = 0 \quad (7b)$$

where C is the capacitance of chambers and L_1 (L_2) is the inductance of the first (second) Helmholtz resonator of the diatomic unit cell. The pressure in the first (second) chamber of the i th unit cell is denoted by p_i (q_i). Introducing $\omega_1 = 1/\sqrt{CL_1}$ ($\omega_2 = 1/\sqrt{CL_2}$) as the fundamental frequency of the first (second) Helmholtz resonator, we further simplify the governing equations to get:

$$(\omega_1^2 + \omega_2^2 - \omega^2) p_i - (\omega_1^2 q_i + \omega_2^2 q_{i-1}) = 0 \quad (8a)$$

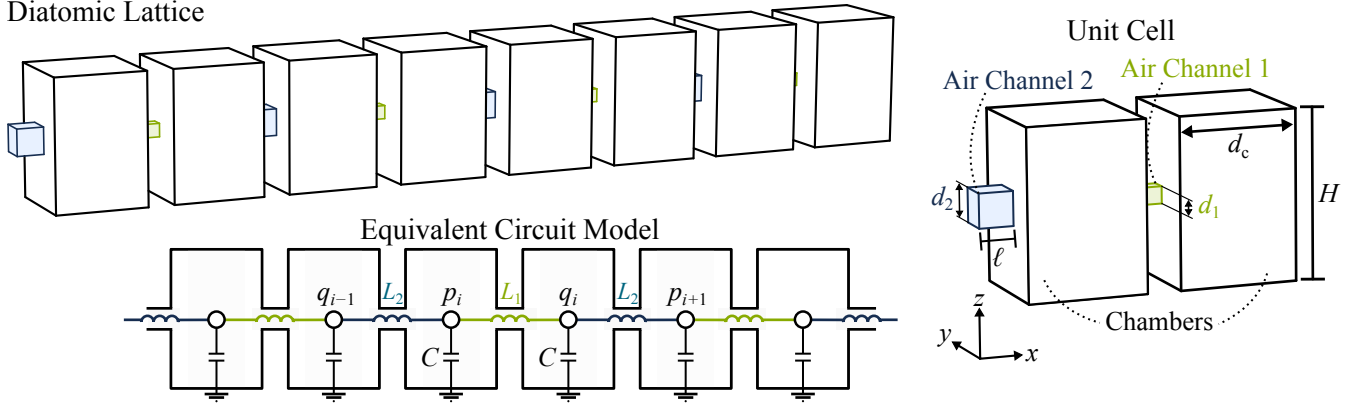


Figure 3: Schematics for an acoustic diatomic lattice, its equivalent electrical circuit model, and its unit cell definition with detailed geometrical properties. Note that chambers (channels) are of square cross-sectional area with sides d_c ($d_{1,2}$).

$$(\omega_1^2 + \omega_2^2 - \omega^2) q_i - (\omega_1^2 p_i + \omega_2^2 p_{i+1}) = 0 \quad (8b)$$

Finally, applying the Bloch theorem yields an eigenvalue problem:

$$\mathbf{H} \mathbf{p}_i = \omega^2 \mathbf{p}_i \quad (9)$$

where the unit-cell's Hamiltonian \mathbf{H} and pressure vector \mathbf{p}_i , respectively, are:

$$\mathbf{p}_i^T = \{p_i \ q_i\} \quad (10a)$$

$$\mathbf{H} = \begin{bmatrix} \omega_1^2 + \omega_2^2 & -\omega_1^2 - \omega_2^2 e^{-i\mu} \\ -\omega_1^2 - \omega_2^2 e^{i\mu} & \omega_1^2 + \omega_2^2 \end{bmatrix} \quad (10b)$$

It is straightforward to compute the eigenvalues from $|\mathbf{H} - \omega^2 \mathbf{I}| = 0$, which results in the dispersion branches:

$$\omega = \sqrt{\omega_1^2 + \omega_2^2 \pm \sqrt{\omega_1^4 + \omega_2^4 + 2\omega_1^2 \omega_2^2 \cos(\mu)}} \quad (11)$$

Figure 4A shows the analytical dispersion branches that are computed directly from Equation (11) by sweeping the values of the wavenumber in the Brillouin zone, i.e., $\mu \in [-\pi, \pi]$, for the cases of (i) $\omega_2 < \omega_1$, (ii) $\omega_2 = \omega_1$ and (iii) $\omega_2 > \omega_1$. Superimposed are the numerically obtained dispersion relation (presented as circles), displaying excellent agreement with their analytical counterpart (presented as lines). We change the values of $\omega_{1,2}$ by introducing the parameterization $d_{1,2} = d_0 \mp \Delta d/2$, where Δd is the difference in channel's hydraulic diameter and $d_0 = (d_1 + d_2)/2$. In this example, we choose $\Delta d = -1, 0, +1$ mm, which give (i) $d_1 = 3.5$ mm and $d_2 = 2.5$ mm, (ii) $d_1 = d_2 = 3$ mm, and (iii) $d_1 = 2.5$ mm and $d_2 = 3.5$ mm, respectively. Chamber's height and side length (diameter) are $H = 20$ mm and $d_c = 14$ mm, respectively, and they remain unchanged throughout. As expected, a bandgap opens only for $\omega_2 \neq \omega_1$ and its limits are $\omega = \sqrt{2}\omega_1$ and $\omega = \sqrt{2}\omega_2$, which are computed from the dispersion relation at the Brillouin zone edge $\mu = \pm\pi$ (Fig. 4B). Moreover, the first (Fig. 4A(i)) and last (Fig. 4A(iii)) dispersion relations have no apparent difference as they signify a different choice of the unit cell by flipping the order of narrow/wide channels, which warrants an identical dispersion relation as evident from Equation (11). Note that the order of the bandgap limits is contingent on $\omega_{1,2}$ values and, hence, its bandgap width is $\Delta\omega = \sqrt{2}|\omega_1 - \omega_2|$.

3.2 Winding number and edge states

Although the dispersion relations in Fig. 4A(i,iii) are identical, a deeper look into their band topology would reveal that they are, in truth, topologically distinct. To attain an insight of the topological properties of the lattice, we re-write the Hamiltonian as a summation of Pauli matrices:

$$\mathbf{H} = - \sum_l h_l \sigma_l \quad (12)$$

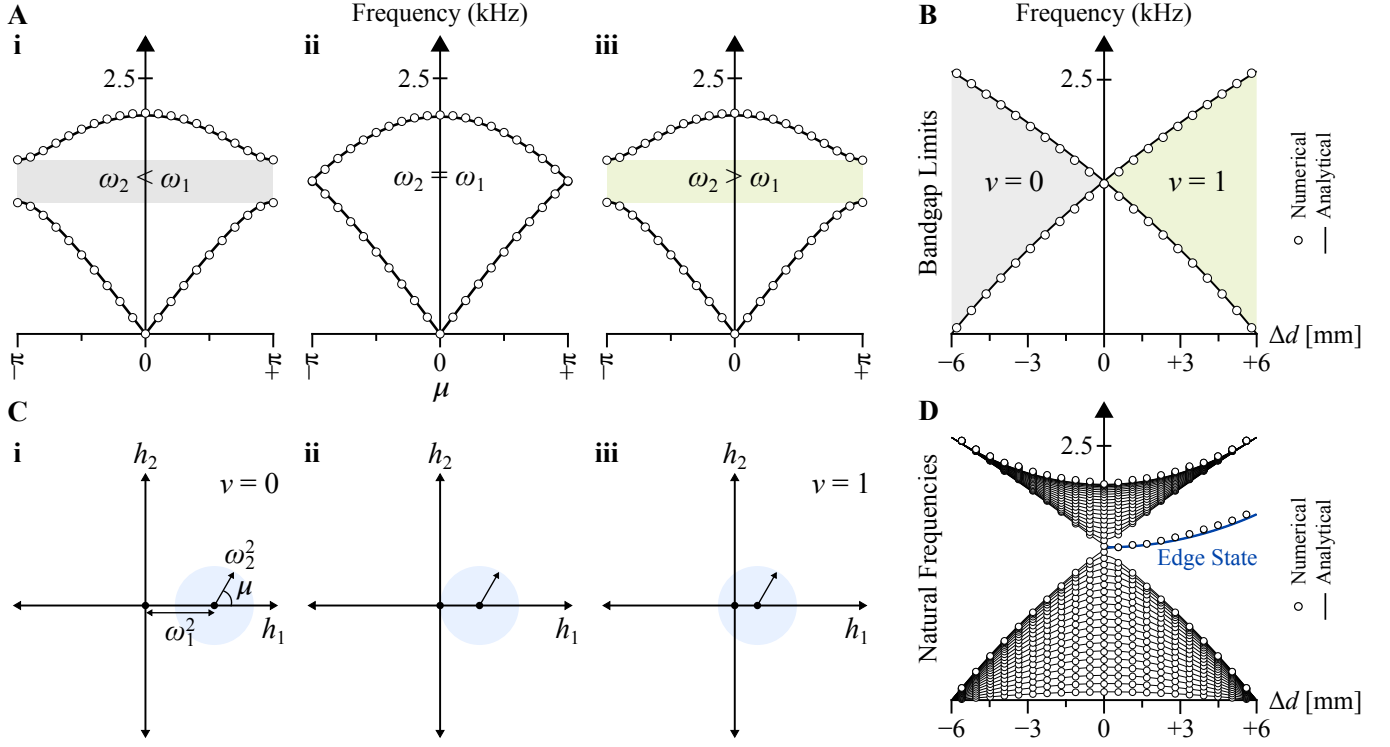


Figure 4: (A) Dispersion relations for diatomic lattices with the following three combinations of the Helmholtz resonance frequencies: (i) $\omega_2 < \omega_1$, (ii) $\omega_2 = \omega_1$, and (iii) $\omega_2 > \omega_1$. (B) Bandgap limits showing the transition of the winding number with the bandgap closing when $\omega_2 = \omega_1$ (i.e., $\Delta d = 0$). As long as the bandgap remains open, the winding number does not change. (C) Functions h_1 versus h_2 , showing the corresponding winding number associated with their oriented path, similar to elastic diatomic lattices [27]. (D) Natural frequency distribution of a finite acoustic chain of 40 chambers with open-open boundary conditions, showing the emergence of doubly degenerate edge states when the winding number is non-zero. All simulations show an excellent agreement between analytical and numerical results.

where $l = 0, 1, 2, 3$ and

$$h_0 = -(\omega_1^2 + \omega_2^2) \quad (13a)$$

$$h_1 = \omega_1^2 + \omega_2^2 \cos(\mu) \quad (13b)$$

$$h_2 = \omega_2^2 \sin(\mu) \quad (13c)$$

$$h_3 = 0 \quad (13d)$$

Note here that the zeroth Pauli matrix σ_0 is a 2×2 identity matrix. In this class of periodic systems, a quantized winding number, denoted as ν , is sought to achieve a topologically protected edge state. To guarantee such quantization, the diagonal of the Hamiltonian for the diatomic chain must be constant, suggesting that σ_3 does not play any role in the Hamiltonian [28]. This condition is already satisfied by setting equal capacitance C , which ultimately returns $h_3 = 0$ as evident from Equation (13). The meaning of the winding number can be interpreted graphically from plotting h_1 versus h_2 , as functions of μ , which gives a perfect circle of radius ω_2^2 with its center shifted by ω_1^2 from the origin. If the depicted circle winds the origin once, as in the case of $\omega_2 > \omega_1$, the winding number shall be $\nu = 1$. However, the circle does not wind the origin for the $\omega_2 < \omega_1$, resulting in $\nu = 0$. The transition between the two cases occurs when $\omega_2 = \omega_1$ such that the circle touches the origin and the winding number becomes undefined (Fig. 4C). It is rather interesting to note that, unlike elastic diatomic lattice that requires equal masses to achieve quantized winding numbers [27, 29, 30], the acoustic diatomic lattice requires constant capacitance (mechanically equivalent to the reciprocal of stiffness) and different inductance (mechanically equivalent to mass) to achieve said quantization. It is also worth noting that elastic diatomic lattice has identical behavior observed in Fig. 4C, albeit that the circle radius and distance are related to the lattice's spring constants [27].

A quantized winding number dictates the emergence, or the lack thereof, of topological edge states at the boundaries of a chain with a finite number of unit cells, n . As the boundary of a finite chain is well-defined, unlike the infinite case where the structure is theoretically unbounded, the distinction between the cases of $\omega_2 > \omega_1$ or $\omega_2 < \omega_1$ is

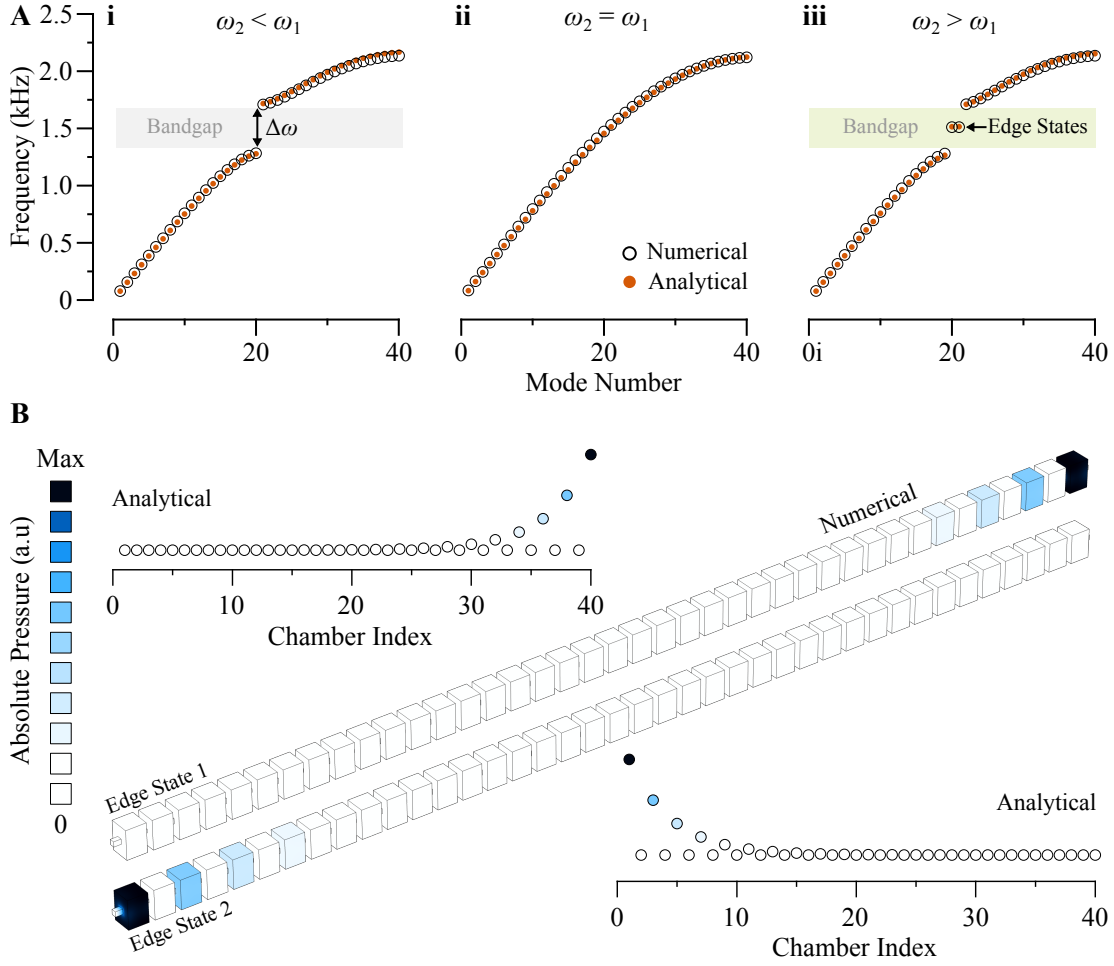


Figure 5: Natural frequency spectrum for three different acoustic diatomic lattices, showing the emergence of edge states only when $\omega_2 > \omega_1$, following the band topology analysis in Fig. 4. The mode shapes of these topological states are also depicted for the full-scale three-dimensional model and compared to the ones obtained from the analytical one.

unambiguous. Therefore, we consider a finite acoustic diatomic lattice that is terminated at channels with hydraulic diameter of d_2 from both ends. The boundary conditions at both ends are open, i.e., the pressure of peripheral chambers is connected to a node with zero oscillatory pressure via an L_2 inductor. Following a similar parametrization procedure to that in the unit cell analysis, the unforced response of the lattice, in frequency domain, is governed by:

$$[\mathbf{D} - \omega^2 \mathbf{I}] \mathbf{p}(\omega) = \mathbf{0} \quad (14)$$

where the degrees of freedom are the acoustic pressure in chambers and read:

$$\mathbf{p}(\omega) = \{p_1 \ q_1 \ p_2 \ q_2 \ \dots \ p_n \ q_n\}^T \quad (15)$$

The matrix \mathbf{D} is a tridiagonal 2-Toeplitz matrix of size $2n \times 2n$ that dictates the dynamical characteristics of the acoustic system and is solely a function of $\omega_{1,2}$:

$$\mathbf{D} = (\omega_1^2 + \omega_2^2) \mathbf{I}_{2n} - \mathbf{\Omega} \quad (16)$$

where $\mathbf{I}_{[\cdot]}$ is an identity matrix with its size indicated in the subscript and

$$\mathbf{\Omega} = \begin{bmatrix} 0 & \omega_1^2 & 0 & \dots & 0 \\ \omega_1^2 & 0 & \omega_2^2 & \ddots & \vdots \\ 0 & \omega_2^2 & \ddots & \ddots & 0 \\ \vdots & \ddots & \ddots & \ddots & \omega_1^2 \\ 0 & \dots & 0 & \omega_1^2 & 0 \end{bmatrix} \quad (17)$$

It is worth noting that the structure of \mathbf{D} resembles the dynamical matrix of an elastic diatomic lattice with fixed-fixed boundary conditions [31]. Numerically solving the eigenvalues of matrix \mathbf{D} for swept values of Δd (thus simultaneously changing ω_1 and ω_2) reveal the emergence of edge modes, which are pinned at:

$$\omega = \sqrt{\omega_1^2 + \omega_2^2} \quad (18)$$

only when $d_2 > d_1$ (or $\omega_2 > \omega_1$). The latter is expected in accordance to the non-vanishing winding number from band topology predictions. These analytical results are compared to the numerical ones obtained from COMSOL simulations. To avoid discrepancies in computed natural frequencies in the numerical problem, the length of both open-end channels must be adjusted by considering the effective length ℓ_e rather than the nominal theoretical one ℓ . Recall that the effective length for a Helmholtz resonator's neck is achieved from adding two corrections: one for the inner side (connected to the chamber with correction factor $\delta_{\text{in}} = 0.425d_h/\ell$) and one for the outside open side (with correction factor $\delta_{\text{out}} = 0.3d_h/\ell$). As such, the correction for end channels needs to be modified only for the outside (open) end, given that the inner side correction is already accounted for in the three-dimensional model. That is, the open channels at both lattice ends should have an effective length of $\ell(1 + \delta_{\text{out}})$. Taking a channel's hydraulic diameter of $d_2 = 3.5\text{mm}$ as a case in point, the effective length evaluates to $\ell_e = 5.05\text{mm}$. Setting up the numerical problem as described above, the overall distribution of the natural frequencies from the numerical solution excellently match those from the analytical model (Fig. 4D). This is further emphasized from the mode shapes for the in-gap edge states, which shows wave localization at edges with strong wave attenuation away from them, as expected. Figure 5 also evinces the agreement in the mode shapes of the numerical three-dimensional model with their analytical counterpart. Note that the results in Fig. 5 are obtained using identical parameter set to that in Fig. 4A.

4 Acoustic honeycomb lattices

4.1 Dispersion surfaces and unit-cell Hamiltonian

Next, consider an acoustic honeycomb lattice and its unit cell equivalent circuit model (Fig. 6A,B). We assign the chamber pressure of the first and second chambers of the i, j unit cell to be $p_{i,j}$ and $q_{i,j}$, respectively, and the impedance of the channels to be $i\omega L$, where L is the equivalent inductance of the connecting channels and is constant throughout (Fig. 6B). The two chambers of the unit cell, on the other hand, are assigned different heights H_1 and H_2 , yielding distinct equivalent capacitance of C_1 and C_2 , respectively. As such, the governing equations of a unit cell are given by:

$$\left(\frac{3}{i\omega L} + i\omega C_1\right) p_{i,j} - \frac{1}{i\omega L} (q_{i,j} + q_{i-1,j} + q_{i,j-1}) = 0 \quad (19a)$$

$$\left(\frac{3}{i\omega L} + i\omega C_2\right) q_{i,j} - \frac{1}{i\omega L} (p_{i,j} + p_{i+1,j} + p_{i,j+1}) = 0 \quad (19b)$$

Applying Bloch theorem and introducing

$$\omega_{1,2} = \sqrt{1/(LC_{1,2})} \quad (20a)$$

$$\varepsilon = 1 + e^{i\mu_+} + e^{i\mu_-} \quad (20b)$$

$$\mu_{\pm} = \frac{1}{2} \left(\sqrt{3}\mu_y \pm \mu_x \right) \quad (20c)$$

the degrees of freedom in Equation (19) can be condensed and cast into a similar matrix form to Equation (9) with:

$$\mathbf{H} = \begin{bmatrix} 3\omega_1^2 & -\omega_1^2 \varepsilon^\dagger \\ -\omega_2^2 \varepsilon & 3\omega_2^2 \end{bmatrix} \quad (21a)$$

$$\mathbf{p}_{i,j} = \{p_{i,j} \quad q_{i,j}\}^T \quad (21b)$$

The dimensionless wavenumbers μ_{\pm} are function of μ_x and μ_y , defined as the wavenumbers in the x - and y - directions, respectively. By defining $E(\mu_+, \mu_-) = (\cos(\mu_+) + \cos(\mu_-) + \cos(\mu_+ - \mu_-) - 3)$, the associated eigenvalues of \mathbf{H} dictating the dispersion surfaces are expressed in the following compact form:

$$\omega = \sqrt{\frac{3}{2}(\omega_1^2 + \omega_2^2) \pm \sqrt{\frac{9}{4}(\omega_1^2 + \omega_2^2)^2 + 2\omega_1^2\omega_2^2 E(\mu_+, \mu_-)}} \quad (22)$$

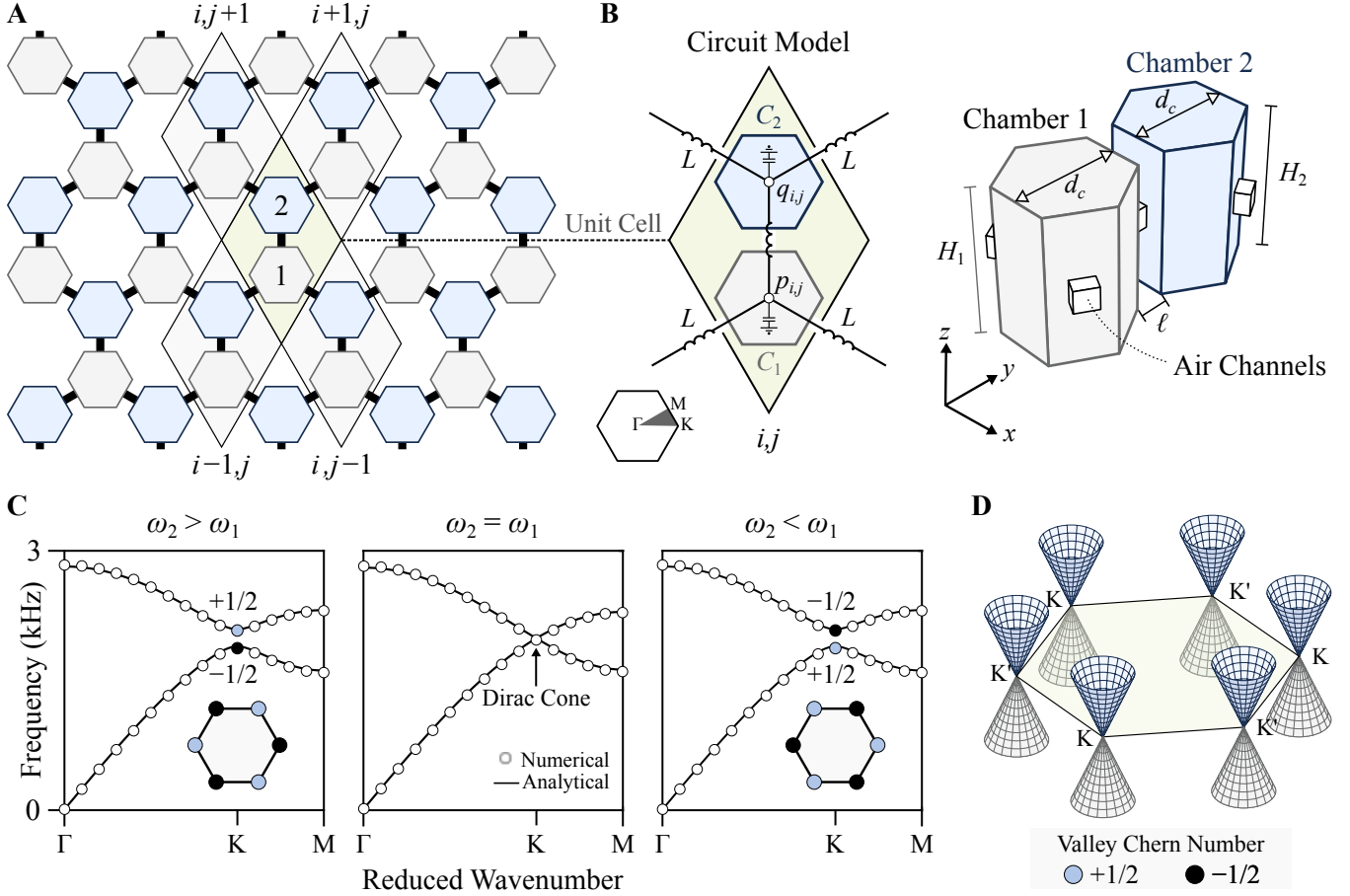


Figure 6: (A,B) Schematics of an acoustic honeycomb lattice, the unit cell definition, and the equivalent circuit model of the unit cell. Note that the change in the chamber height occurs symmetrically from both z -directions, such that the channels remain always centered with respect to the chambers. (C) Dispersion diagrams for $\Delta H = H_2 - H_1 = \pm 4, 0$ mm showing that valley Hall transition, dictated by flipping the sign of the valley Chern number (blue circles are $+1/2$ and black circles are $-1/2$). The transition occurs exactly at $\Delta H = 0$ and a Dirac cone is generated. (D) The corresponding linearized Hamiltonian at the corners of the Brillouin zone gives perfect cones at K (K') points.

It is observed that the Hamiltonian in Equation (21a) is not symmetric, thus cannot be expressed in terms of Pauli matrices. To achieve such a symmetric Hamiltonian and properly interpret topological properties, we introduce a new basis $\hat{\mathbf{p}} = \mathbf{Q}\mathbf{p}_{i,j}$, parallel to the methodology presented in Ref. [30], with the definition of the transformation matrix \mathbf{Q} being:

$$\mathbf{Q} = \text{diag} [1/\omega_1 \quad 1/\omega_2] \quad (23)$$

As such, we arrive at the following eigenvalue problem,

$$\hat{\mathbf{H}}\hat{\mathbf{p}} = \omega^2\hat{\mathbf{p}} \quad (24)$$

where

$$\hat{\mathbf{H}} = \begin{bmatrix} 3\omega_1^2 & -\omega_1\omega_2\epsilon^\dagger \\ -\omega_1\omega_2\epsilon & 3\omega_2^2 \end{bmatrix} \quad (25)$$

The Hamiltonian in Equation (25) can be now expressed as a summation of Pauli matrices, i.e., Equation (12), with the following parameters:

$$h_0 = -3(\omega_1^2 + \omega_2^2)/2 \quad (26a)$$

$$h_1 = \omega_1\omega_2 (1 + \cos(\mu_+) + \cos(\mu_-)) \quad (26b)$$

$$h_2 = \omega_1\omega_2 (\sin(\mu_+) + \sin(\mu_-)) \quad (26c)$$

$$h_3 = -3(\omega_1^2 - \omega_2^2)/2 \quad (26d)$$

A key parameter here is h_3 and its presence results in breaking the inversion symmetry [32]. The latter forces a frequency bandgap to open (when $\omega_1 \neq \omega_2$) and its limits are found from the solutions of dispersion relation at K point (or equivalently K' point), i.e., $(\mu_x^K, \mu_y^K) = (4\pi/3, 0)$, resulting in $\omega = \sqrt{3}\omega_{1,2}$ (Fig. 6C).

4.2 Valley Chern number

Breaking inversion symmetry and maintaining a third order rotational symmetry give rises to QVHE [30, 32]. The topological invariant quantifying topological transition is the valley Chern number C_v , which is calculated based on a linearized version of the Hamiltonian in Equation (25) near a Dirac cone. The latter is simply achieved by expanding the function ε via a multi-variable Taylor series near the K point,

$$\delta\varepsilon = \varepsilon + \frac{\partial\varepsilon}{\partial\mu_x}\delta\mu_x + \frac{\partial\varepsilon}{\partial\mu_y}\delta\mu_y \quad (27)$$

where $\delta\mu_x(\delta\mu_y)$ are wavenumbers measured from $\mu_x^K(\mu_y^K)$. Analogous procedure can be followed for the complex conjugate ε^\dagger . Evaluating the expression at the K point and knowing that $\varepsilon(\mu_x^K, \mu_y^K) = 0$, Equation (27) boils down to:

$$\delta\varepsilon = -\frac{\sqrt{3}}{2}(\tau\delta\mu_x + \delta\mu_y) \quad (28)$$

where $\tau = +1(-1)$ for the K(K') point. Subsequently, the linearized Hamiltonian, while ignoring the constant diagonal entries (i.e., $h_0\sigma_0$), can be written as [33]:

$$\delta\mathbf{H} = v_D(\tau\delta\mu_x\sigma_1 + \delta\mu_y\sigma_2) + m_Dv_D^2\sigma_3 \quad (29)$$

where v_D and m_D are the Dirac velocity and effective mass, respectively. For our specific configuration, v_D and m_D are given by:

$$v_D = \frac{\sqrt{3}}{2}\omega_1\omega_2 \quad (30a)$$

$$m_D = 2\frac{(\omega_1^2 - \omega_2^2)}{(\omega_1\omega_2)^2} \quad (30b)$$

Based on the linearized Hamiltonian $\delta\mathbf{H}$, we examine the following eigenvalue problem:

$$\delta\mathbf{H}\delta\mathbf{p} = \delta\omega^2\delta\mathbf{p} \quad (31)$$

with the following eigenpair:

$$\delta\omega = \pm v_D\sqrt{(m_Dv_D)^2 + \delta\mu_x^2 + \delta\mu_y^2} \quad (32a)$$

$$\delta\mathbf{p} = \{m_Dv_D^2 \pm |\delta\omega^2| \quad v_D(\tau\delta\mu_x + \mathbf{i}\delta\mu_y)\}^T \quad (32b)$$

It is important to point out that if $m_D = 0$, i.e., $\omega_1^2 = \omega_2^2 = \omega_0^2$, the eigenvalues in Equation (32a) describe perfect cones (Fig. 6D):

$$\delta\omega = \pm\frac{1}{2}\omega_0\sqrt{3(\delta\mu_x^2 + \delta\mu_y^2)} \quad (33)$$

which has been similarly established for an in-plane Kagome elastic lattice [27]. The eigenvectors in Equation (32b) are crucial to calculate the Berry curvature, which, after normalizing $\delta\mathbf{p}_\pm$, can be shown to be [34]:

$$\mathcal{F}_\pm = \frac{\mp\tau m_D v_D}{2(m_D^2 v_D^2 + \delta\mu_x^2 + \delta\mu_y^2)^{3/2}} \quad (34)$$

Finally, the integration of Berry curvature near a single valley yields a quantized Valley Chern number:

$$C_v^\pm = \mp\frac{1}{2}\mathbf{sgn}[m_D] \quad (35)$$

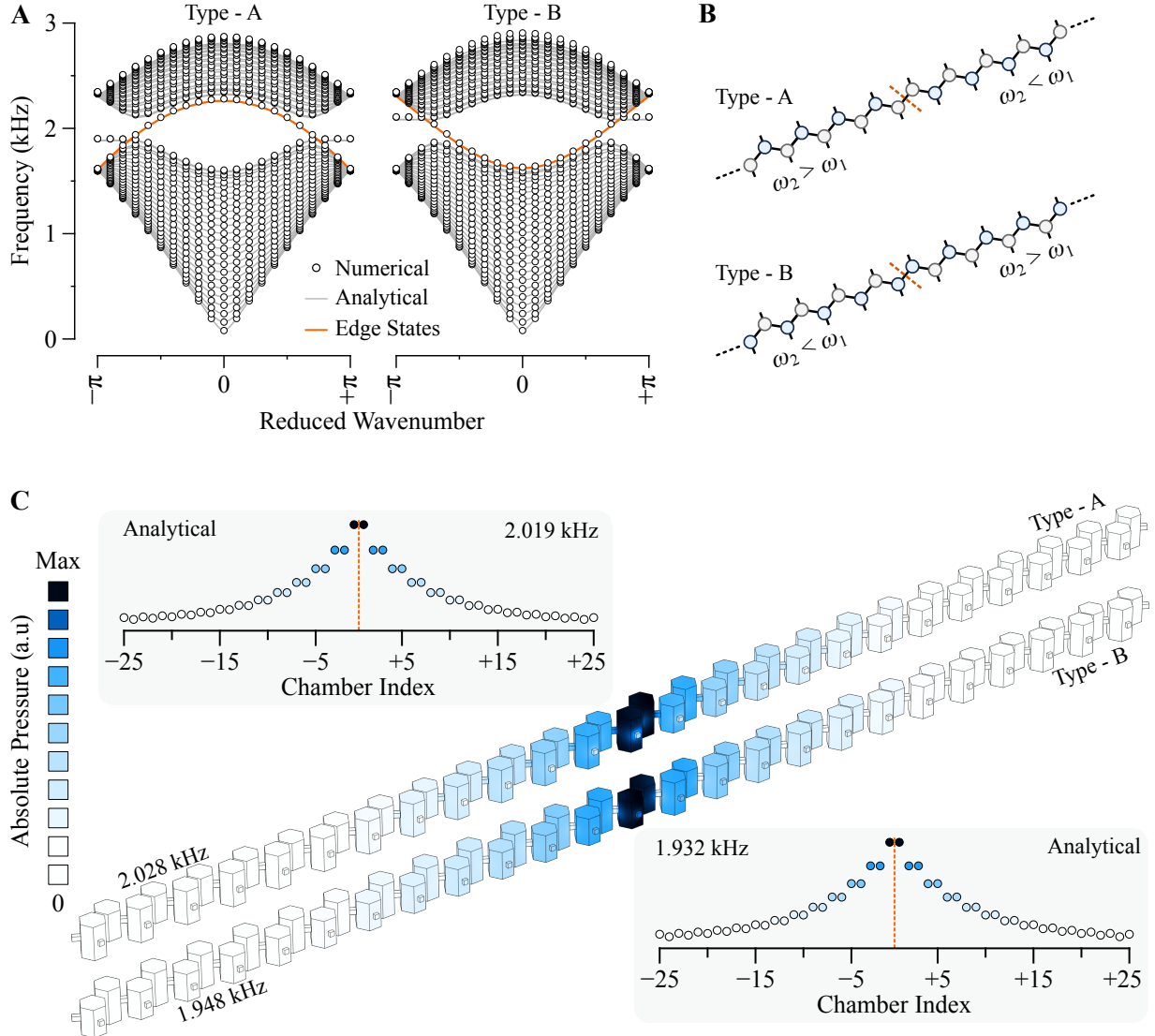


Figure 7: (A,B) Supercell analysis for a honeycomb lattice, formed by merging two lattices with flipped order of chambers at an interface midway, with 25 chambers on each side. The spectrum based on the full-scale numerical model (circles) and analytical one (lines) are shown for two types of interface modes (orange lines): Type-A (large chambers interface) and Type-B (small chambers interface). (C) Corresponding eigenmodes at reduced wavenumber of 0.6π based on the numerical and analytical models.

4.3 Finite lattice dynamics and waveguide design

One of the implications of having topological transition dictated by the sign of C_v is to design robust interface modes and waveguides. This can be demonstrated by performing standard supercell dispersion analysis on a single strip of the honeycomb lattice with flipped order of the lattice chambers at a midway interface with a second dimension being infinite (Fig. 7A,B). This configuration results in a lattice with two parts having opposite signs of C_v , and, consequently, there should exist a single in-gap interface mode [35]. Performing such analysis in a chain of 50 chambers and $\Delta H = H_1 - H_2 = \pm 4\text{mm}$, we observe an interface mode (depicted in orange in Fig. 7A) in both the analytical and numerical (three-dimensional) models, with an overall agreement. The nature of such interface modes is further confirmed by examining the mode shape; for example, Fig. 7C shows the absolute pressure of an in-gap mode at a reduced wavenumber of 0.6π , which, again, shows an excellent agreement between the analytical and numerical models. Note here that the left/right boundaries are terminated at an open channel on both lattice's ends and the length of peripheral channels are adjusted in a similar way to that of the diatomic lattice in Fig. 5.

Based on the supercell analysis, we now devise waveguides with L- and Z- shapes in a parallelogram-like lattice (Fig. 8). The acoustic lattice is built from $n = 25$ rows of diatomic lattice strips (as in Fig. 7B), with each strip having an n unit cells, to form a parallelogram-like honeycomb lattice with a total of $n_t = 2n^2 = 1250$ chambers. We simulate two

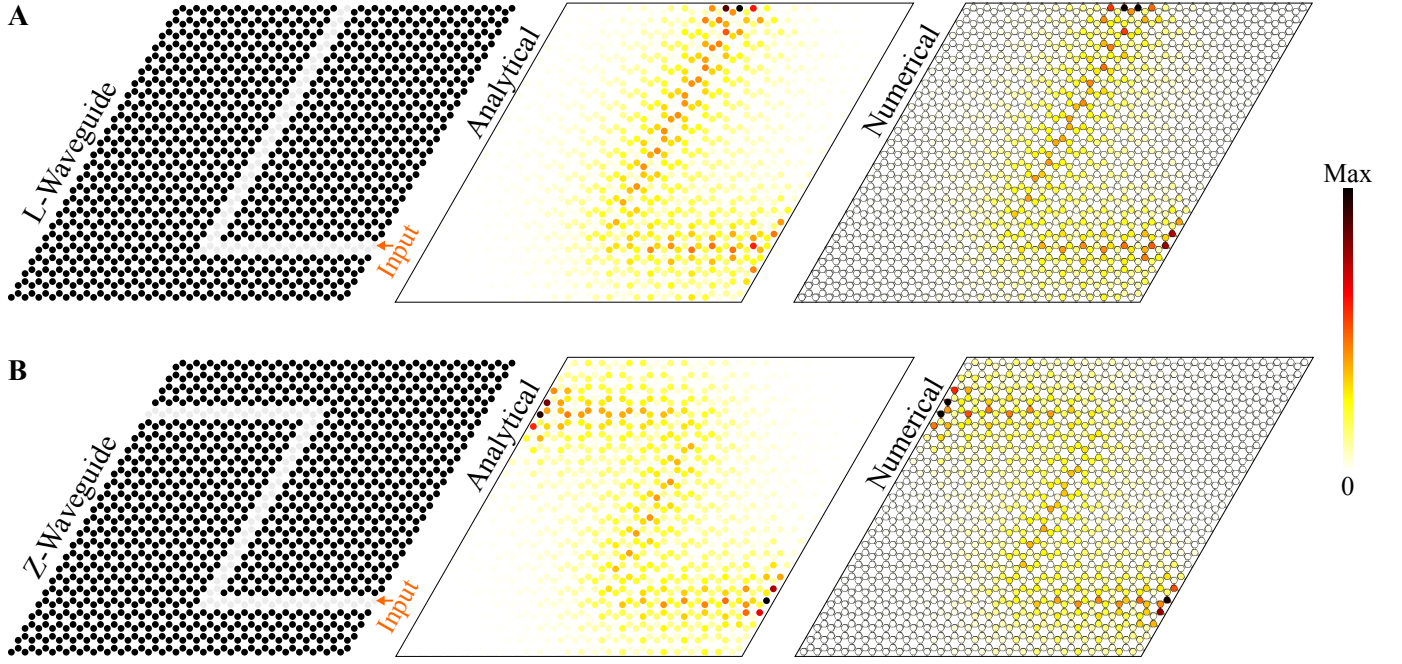


Figure 8: A parallelogram shaped honeycomb structure with embedded (A) L- and (B) Z-waveguides. An arbitrary input is imposed on the right end of the waveguide at a frequency of 2kHz (around the center of the frequency bandgap). The numerical and analytical models show qualitatively similar behavior.

waveguides of L- and Z-shapes (Fig. 8A,B) and compute the system response to an arbitrary excitation with a frequency of 2kHz at the right end of the waveguide. It is evident from the results that the pressure is localized at the waveguide, precisely as predicted from the supercell analysis in Fig. 7C. Both the numerical and analytical models are in perfect agreement, which demonstrates the power of the analytical model, while having a much smaller number of degrees of freedom, all without any apparent difference in the overall response.

5 Conclusions

This paper has established the use of electroacoustic analogies for designing acoustic topological lattices. The physical meaning of the parameters established from the effective Hamiltonian is related to Helmholtz resonance, allowing for a better estimation of its frequency based on geometrical properties. The benefit of the established platform is its less demand of numerical computation, in comparison to a full-scale model that typically increases the computation cost several folds. We show the potential and effectiveness of such approach via two examples of topological systems: (i) An acoustic diatomic lattice with edge states and quantized winding numbers. (ii) An acoustic honeycomb lattice with embedded topological waveguides emanating from QVHE. Both cases show excellent agreement between the analytical circuit model and the full-scale three-dimensional one, whether in finite lattice frequency response or unit-cell based analyses. The simplicity and computational efficiency of the established framework can be invaluable for designing various acoustic topological lattices in the future.

Acknowledgement

The authors acknowledge the funding support from the United States Air Force Office of Scientific Research (FA9550-18-1-0192).

References

- [1] X. Zhang, M. Xiao, Y. Cheng, M.-H. Lu, J. Christensen, *Communications Physics* **2018**, 1, 97.
- [2] G. Ma, M. Xiao, C. T. Chan, *Nature Reviews Physics* **2019**, 1, 281–294.
- [3] C. He, X. Ni, H. Ge, X.-C. Sun, Y.-B. Chen, M.-H. Lu, X.-P. Liu, Y.-F. Chen, *Nature Physics* **2016**, 12, 1124–1129.
- [4] J. Lu, C. Qiu, L. Ye, X. Fan, M. Ke, F. Zhang, Z. Liu, *Nature Physics* **2017**, 13, 369–374.
- [5] J.-P. Xia, D. Jia, H.-X. Sun, S.-Q. Yuan, Y. Ge, Q.-R. Si, X.-J. Liu, *Advanced Materials* **2018**, 30, 1805002.
- [6] H. He, C. Qiu, L. Ye, X. Cai, X. Fan, M. Ke, F. Zhang, Z. Liu, *Nature* **2018**, 560, 61–64.
- [7] X. Ni, M. A. Gorlach, A. Alu, A. B. Khanikaev, *New Journal of Physics* **2017**, 19, 055020.
- [8] A. B. Khanikaev, R. Fleury, S. H. Mousavi, A. Alù, *Nature Communications* **2015**, 6, 8260.
- [9] Y. Yang, Z. Yang, B. Zhang, *Journal of Applied Physics* **2018**, 123, 091713.
- [10] M. Gao, S. Wu, J. Mei, *New Journal of Physics* **2020**, 22, 013016.
- [11] X. Ni, K. Chen, M. Weiner, D. J. Apigo, C. Prodan, A. Alu, E. Prodan, A. B. Khanikaev, *Communications Physics* **2019**, 2, 1–7.
- [12] H. Xue, Y. Yang, F. Gao, Y. Chong, B. Zhang, *Nature Materials* **2019**, 18, 108–112.
- [13] Y. Qi, C. Qiu, M. Xiao, H. He, M. Ke, Z. Liu, *Physical Review Letters* **2020**, 124, 206601.
- [14] X. Ni, M. Li, M. Weiner, A. Alù, A. B. Khanikaev, *Nature Communications* **2020**, 11, 2108.
- [15] A.-Y. Guan, Z.-Z. Yang, X.-Y. Zou, J.-C. Cheng, *Physical Review Applied* **2021**, 15, 064056.
- [16] M. Nouh, O. Aldraihem, A. Baz, *Journal of Dynamic Systems Measurement and Control* **2014**, 136, 061005.
- [17] S. Zhang, *Acoustic metamaterial design and applications*, University of Illinois at Urbana-Champaign, **2010**.
- [18] A. Roshwalb, M. Nouh, O. Aldraihem, A. Baz, *Journal of intelligent material systems and structures* **2014**, 25, 1372–1383.
- [19] W. Akl, A. Baz, *Journal of intelligent material systems and structures* **2010**, 21, 541–556.
- [20] W. Akl, A. Baz, *Journal of dynamic systems measurement and control* **2012**, 134, 061001.
- [21] H. Al Ba’ba’a, J. Callanan, M. Nouh, T. Singh, *Meccanica* **2018**, 53, 3105–3122.
- [22] J. Yuan, *Journal of Vibration and Acoustics* **2007**, 129, 94–100.
- [23] M. Alster, *Journal of Sound and Vibration* **1972**, 24, 63–85.
- [24] M. Xu, A. Selamet, H. Kim, *Applied Acoustics* **2010**, 71, 822–829.
- [25] D. R. Raichel, *The science and applications of acoustics*, Springer Science & Business Media, **2006**.
- [26] P. Wibulswas, PhD thesis, University of London, **1966**.
- [27] H. Chen, H. Nassar, G. L. Huang, *Journal of the Mechanics and Physics of Solids* **2018**, 117, 22–36.
- [28] J. K. Asbóth, L. Oroszlány, A. Pályi, *A Short Course on Topological Insulators*, Springer International Publishing, Cham, **2016**, pp. 997–1000.
- [29] R. K. Pal, J. Vila, M. Leamy, M. Ruzzene, *Physical Review E* **2018**, 97, 32209.
- [30] R. K. Pal, M. Ruzzene, *New Journal of Physics* **2017**, 19, 25001.
- [31] H. Al Ba’ba’a, M. Nouh, T. Singh, *The Journal of the Acoustical Society of America* **2017**, 142, 1399–1412.
- [32] H. Al Ba’ba’a, K. Yu, Q. Wang, *Extreme Mechanics Letters* **2020**, 38, 100758.
- [33] Z. Tian, C. Shen, J. Li, E. Reit, H. Bachman, J. E. Socolar, S. A. Cummer, T. Jun Huang, *Nature Communications* **2020**, 11, 762.
- [34] Y. Chen, X. Liu, G. Hu, *Journal of the Mechanics and Physics of Solids* **2019**, 122, 54–68.
- [35] E. Riva, D. E. Quadrelli, G. Cazzulani, F. Braghin, *Journal of Applied Physics* **2018**, 124, 164903.